



Highly selective conversion of CO_x to C₂₋₄ hydrocarbons over MoS_x@HSSZ-39 catalyst

Taotao Zhao^a, Yuchi Liu^a, Chenyang Shen^a, Gui Liu^a, Jun Yao^a, Xiaofeng Qian^a, Qiang He^a, Feifei Mei^a, Deming Meng^a, Xuefeng Guo^a, Luming Peng^a, Nianhua Xue^{a,*}, Yan Zhu^a, Yuming Zhou^b, Weiping Ding^{a,*}

^a Key Lab of Mesoscopic Chemistry, School of Chemistry and Chemical Engineering, Nanjing University, Nanjing 210023, China

^b School of Chemistry and Chemical Engineering, Southeast University, Nanjing 211189, China

ARTICLE INFO

Keywords:

CO_x hydrogenation

Low hydrocarbons

Bifunctional

MoS_x

HSSZ-39 zeolite

ABSTRACT

Here, we report a high-performance catalyst MoS_x@HSSZ-39 for conversion of CO_x to C₂₋₄ hydrocarbons, in which MoS_x clusters for CO_x hydrogenation at the first to intermediate methanol and then the zeolitic acid sites surrounding for further conversion of methanol to hydrocarbons. For CO₂ hydrogenation, C₂₋₄ hydrocarbons of ~90% selectivity in organic products at 32.7% of CO₂ conversion and excellent stability of 1000 h on stream are obtained. For CO hydrogenation, 95% of C₂₋₄ hydrocarbons, 83% of LPG or 74% of propane selectivities at > 22% CO conversion and stable more than 200 h on stream are obtained. The cooperation among the MoS_x clusters and the zeolitic acid sites constitutes the catalyst of intimate bifunction, which is the key to the high catalytic performance for CO_x hydrogenation.

1. Introduction

As an abundant C1 resource, the hydrogenation of CO₂ provides an optional pathway to produce value-added chemicals such as C₂₊ hydrocarbons with exclusive or high selectivity [1–6]. Proverbially, Fischer-Tropsch synthesis (FTS) is a well-established process for conversion of syngas to C₂₊ hydrocarbons, using such as iron-based catalysts [7–11], which also performs promising catalytic activities in reverse water-gas shift (RWGS) reaction. Developing a modified FTS process that the CO₂ initially is converted into intermediate CO via RWGS reaction, followed by C-C chain propagation via FTS reaction on iron-based catalyst has been reported recently [11–14]. It is recognized that, in terms of chemical energy retention rate of raw materials, the hydrogenation of CO₂ is actually more advantageous than the hydrogenation of CO. In view of this, exploring an alternative CO₂ hydrogenation process for high-selective target product is imperative. Up to now, researches about CO₂ hydrogenation to CH₃OH have acquired inspiring achievements [2,15–20], furthermore, the methanol to hydrocarbon (MTH) process is already mature [21–25]. Hence, the production of C₂₊ hydrocarbons via CO₂ hydrogenation mediated by methanol intermediate appears more reasonable [26–29]. It also has advantages to remove the barrier of carbon deposition on acid zeolite,

which has not been completely overcome as before.

Very recently, the excellent performance of molybdenum-sulfur species catalyzing CO₂ hydrogenation to methanol has been demonstrated. Wang and Deng et al. reported that the CO₂ hydrogenation to methanol on sulfur vacancy-rich MoS₂ was found highly efficient, 94.3% methanol selectivity at CO₂ conversion of 12.5%, and stable for more than 3000 hours at 180 °C [2]. Our group reported that the Mo₃S₄@-NaZSM-5 catalyst (Scheme 1(a)) exhibited more excellent low-temperature (180 °C) catalytic performance for CO₂ hydrogenation to methanol, more than 98% of methanol selectivity at 10.8% of CO₂ conversion, and the catalyst kept stable for more than 1000 h on stream [15].

The HSSZ-39 zeolite, owing to its pear-shaped cage with side opening and straight 8-MR channel structure of zeolite, shows excellent shape-selectivity for small molecule and promising catalytic performance for methanol to olefin (MTO) reaction [30,31]. Inspired by the previous work and considering the stronger confinement effect of the zeolite on species in cages, we elaborately introduce molybdenum sulfide clusters into the channel of acidic zeolite of HSSZ-39 (Scheme 1(b)) to obtain catalyst MoS_x@HSSZ-39 for the direct conversion of CO₂ to C₂₋₄ hydrocarbons.

The MoS_x@HSSZ-39 catalyst is excellent for the reaction. The CO₂

* Corresponding authors.

E-mail addresses: nianhua@nju.edu.cn (N. Xue), dingwp@nju.edu.cn (W. Ding).

<https://doi.org/10.1016/j.apcatb.2024.123936>

Received 11 November 2023; Received in revised form 5 January 2024; Accepted 8 March 2024

Available online 11 March 2024

0926-3373/© 2024 Elsevier B.V. All rights reserved.

conversion reaches 32.7% with C₂₋₄ hydrocarbons selectivity in organic products more than 87% (380 °C, 4 MPa, CO₂/3H₂, 1600 mL g⁻¹·h⁻¹), which keeps stable during 1000 hours on stream. Interestingly, the catalyst is also proved very active for CO hydrogenation to C₂₋₄ hydrocarbons. The selectivity to propane and liquefied petroleum gas (LPG) in organic products exceed 75% and 85%, respectively, at > 22% of CO conversion (350 °C, 4 MPa, CO/2H₂ and 1600 mL g⁻¹·h⁻¹). Similarly, it remains stable during 200 h on stream for the CO hydrogenation. Taking advantages of various characterization techniques, it is found that CO₂ or CO is firstly converted into CH₃OH on the MoS_x sites, verified by the density functional theory (DFT) simulations, then the CH₃OH immediate is further hydrogenated into C₂₋₄ hydrocarbons on the intimate acid sites of HSSZ-39 zeolite.

2. Experimental details

2.1. Chemical reagents

HSSZ-39 zeolite (ratio of Si/Al = 20) was purchased from Nanjing YiMing New Materials Technology Co. Ltd., both MoO₃ (99.5 wt.%) and MoS₂ (99.5 wt.%) were purchased from Aladdin Reagent Co., Ltd., sulfur powder (99.9 wt.%) was purchased from Sigma-Aldrich Reagent Co., Ltd., CH₃COONa (AR 99 wt.%) was purchased from Sinopharm Chemical Reagent Co., Ltd.

2.2. Catalyst preparation

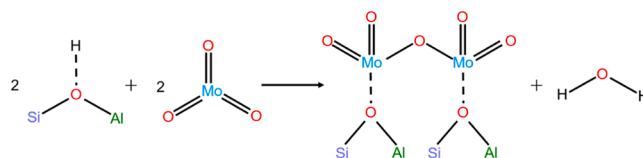
2.2.1. Synthesis of MoS_x@HSSZ-39

Firstly, 1.5 g HSSZ-39 zeolite with Si/Al molar ratio of 20 and 0.0678 g MoO₃ were physically mixed in agate mortar and ground for 40 min for well mixing. Subsequently the mixture was transferred into

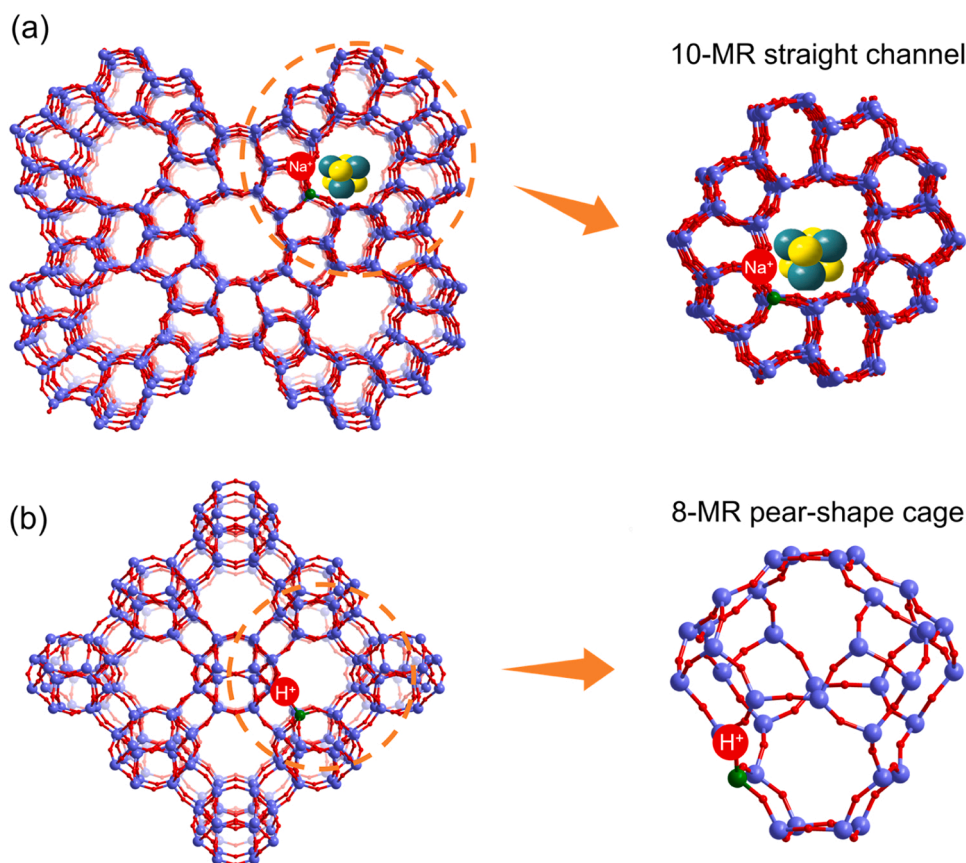
muffle furnace, heated to 650 °C at 10 °C/min and maintained for 30 min at 650 °C. In this step, MoO₃ migrated into the 8-MR channel of HSSZ-39 zeolite, subsequently exchanged with hydroxyl group on the zeolite to form (Mo₂O₅)²⁺ dimer (Scheme 2), of which two Mo atoms fixed at two cation exchange sites in HSSZ-39 zeolite at 650 °C [32–34]. The sample was marked as MoO_x@HSSZ-39. Afterwards, ample sulfur powder and the MoO_x@HSSZ-39 were placed into agate mortar and ground for 30–40 min, subsequently the mixture was transferred into tubular furnace, heated to 500 °C at 10 °C/min and maintained for 240 min at 500 °C under flowing 5% H₂/N₂. The obtained sample was denoted as MoS_x@HSSZ-39 (Mo: 2.95 wt.%, measured by inductively coupled plasma-optical emission spectrometer, ICP-OES).

2.2.2. Synthesis of MoS_y/HSSZ-39

MoS_y/HSSZ-39 (Mo: 2.93 wt.%, measured by ICP-OES) was prepared by one-step method. 1.5 g HSSZ-39 zeolite, 0.0678 g MoO₃ and ample sulfur powder were placed in agate mortar and ground for 30 min. Then the mixture was subsequently introduced into tubular furnace, heated to 400 °C at 10 °C/min and hold for 240 min at 400 °C under flowing 5% H₂/N₂.



Scheme 2. Solid exchange of MoO₃ with hydroxyl groups of HSSZ-39 zeolite.



Scheme 1. Mo₃S₄@NaZSM-5 catalyst [15], the green, red and blue ball in zeolite structure represented framework Al, O and Si atom, respectively (a) and HSSZ-39 zeolite (001) (b).

2.2.3. Synthesis of $\text{MoS}_x\text{@HSSZ-39}$

$\text{MoS}_x\text{@HSSZ-39}$ was dissolved in 1 M CH_3COONa solution and stirred for 120 min at 65 °C. Then the precipitate was filtered out and washed circularly with deionized water, dried overnight at 80 °C in vacuum. The obtained sample finally was marked as $\text{MoS}_x\text{@NaSSZ-39}$.

2.2.4. Synthesis of $\text{MoS}_2\text{+HSSZ-39}$

$\text{MoS}_2\text{+HSSZ-39}$ (Mo: 3 wt.%, obtained from feeding ratio) was directly obtained by physically mixing and grinding 0.0754 g commercial MoS_2 and 1.5 g HSSZ-39 zeolite in agate mortar for 30 min.

2.3. Characterizations

Powders X-ray diffraction (XRD) patterns were recorded from 5 to 60° in 2θ on an X'pert PAN analytical diffractometer with Cu Kα radiation (40 kV, 40 mA). Scanning electron microscopy (SEM) image of sample was obtained through S-4800 field emission SEM with accelerating voltage of 5 kV. The HAADF-STEM images and element distribution of O, Al, Si, S and Mo of $\text{MoS}_x\text{@HSSZ-39}$ was obtained on FEI TalosF200S with accelerating voltage of 200 kV. Spherical-aberration Corrected Scanning Transmission Electron Microscope (STEM) were executed on the Titan Themis G2 at accelerating voltage of 300 kV with integrated Differential Phase Contrast (iDPC) detection modes. The Mo K-edge (20,000 eV) X-ray absorption fine structure (XAFS) analyses were performed at BL14W1 beamline of Shanghai Synchrotron Radiation Facility (Shanghai, China). The EXAFS spectra were processed and analyzed by the software code Athena and corresponding fitted data was obtained from software code Artemis. X-ray photoelectron spectroscopy (XPS) measurement was performed on ThermoFisher ESCALAB250Xi XPS system with Al Kα ($h\nu = 1486.6$ eV) X-ray as exciting source. The content of Mo of sample was recorded by inductively coupled plasma-optical emission spectrometer (ICP-OES) named Agilent 725-ES. The Brunauer-Emmett-Teller (BET) specific surfaces were analyzed with a Micromeritics ASAP2420 analyzer at liquid nitrogen (77 K) temperature, the samples were degassed at 300 °C for 4 hours under 10^{-3} Torr vacuum before the test. Operando Diffused Reflectance Infrared Fourier Transform Spectroscopy (DRIFTS) was recorded by INVENIO S, Bruker spectrometer.

2.4. Catalytic evaluation

CO_2/CO hydrogenation reaction was performed on high-pressure fixed bed reactor equipped with gas chromatograph (GC-9860). Double-layer tube with inner quartz and external stainless-steel tube, respectively, was used as reaction tube. In typical procedure, the powder sample was firstly pressed into 20–40 mesh granule. 0.3 g sample granule (20–40 mesh) was filled in the quartz tube with 0.6 cm inner diameter. In order to avoid the interference of air during reaction and conveniently calculate CO_2/CO conversion after reaction, the feed gas was continuously circulated in the reactor for a period of time under certain pressure before heating up. Finally, the reaction performance of sample for the catalytic hydrogenation of CO_2/CO were systematically investigated. The reaction tail gas was transported to the gas chromatograph (GC-9860) equipped with FID and TCD detector for online analysis under 140 °C. Connecting a Plot Q capillary in front of FID detector and TDX-1 packed column for detecting organic products and CO_2 , Ar, CO gas in the tail gas, respectively. All substances were qualitatively determined by comparing the retention time with the standard. Catalytic data were obtained by using argon (Ar) as the internal standard and the corresponding calculation methods were as follows:

$$\text{CO}_2 \text{ conversion} = \frac{\text{CO}_2^{\text{in}} - \text{CO}_2^{\text{out}}}{\text{CO}_2^{\text{in}}} \times 100\% \quad (1)$$

$$\text{CO conversion} = \frac{\text{CO}^{\text{in}} - \text{CO}^{\text{out}}}{\text{CO}^{\text{in}}} \times 100\% \quad (2)$$

$$\text{CO selectivity} = \frac{\text{CO}^{\text{out}}}{\text{CO}_2^{\text{in}} - \text{CO}_2^{\text{out}}} \times 100\% \quad (3)$$

$$\text{CO}_2 \text{ selectivity} = \frac{\text{CO}_2^{\text{out}}}{\text{CO}^{\text{in}} - \text{CO}^{\text{out}}} \times 100\% \quad (4)$$

C_x hydrocarbons and CH_3OH selectivity in organic products were obtained in Eqs. (5) and (6), respectively.

$$\text{C}_x \text{ selectivity} = \frac{f_{\text{C}_x} \cdot A_{\text{C}_x}}{f_{\text{CH}_3\text{OH}} \cdot A_{\text{CH}_3\text{OH}} + \sum_{i=1}^n f_{\text{C}_i} \cdot A_{\text{C}_i}} \times 100\% \quad (5)$$

$$\text{CH}_3\text{OH selectivity} = \frac{f_{\text{CH}_3\text{OH}} \cdot A_{\text{CH}_3\text{OH}}}{f_{\text{CH}_3\text{OH}} \cdot A_{\text{CH}_3\text{OH}} + \sum_{i=1}^n f_{\text{C}_i} \cdot A_{\text{C}_i}} \times 100\% \quad (6)$$

Where CO_2^{in} , CO^{in} and CO_2^{out} , CO^{out} represented mass of CO_2 and CO at the inlet and outlet, respectively. Letter A and f represented peak area and quality correction factor, respectively.

2.5. DFT calculations

Density functional theory (DFT) simulations were performed using the Vienna *ab initio* simulation package (VASP) code [35,36] with the Perdew-Burke-Ernzerhof (PBE) functional [37]. The inner electrons were described with the projector augmented wave (PAW) pseudopotentials [38], while the valence electrons (i.e., 4p, 4d and 5s for Mo atoms, 3s and 3p for Al, Si and S atoms, 2s and 2p for C and O atoms, and 1s for H atoms) were expanded from a plane-wave basis set with a kinetic energy cutoff of 400 eV. A Γ -centered ($1 \times 1 \times 1$) k -point grid was selected for the integration of the Brillouin zone. All the structures were relaxed until forces on each ion were no more than $0.03 \text{ eV } \text{\AA}^{-1}$, and the convergence criterion for electronic self-consistent interactions was set 10^{-5} . The HSSZ-39 zeolite was modelled using a periodic AEI unit in which part of silica atoms were replaced by aluminum atoms, resulting in the overall Si/Al ratio of 20. During the structural optimization, all the oxygen atoms within the skeleton structure of HSSZ-39 were saturated with hydrogen atoms, and the resultant hydroxyl groups were kept frozen in view of the rigid framework of molecular sieve. The most representative 8-membered ring (8-MR) in AEI was considered for hosting the Mo_3S_4 cluster to construct the $\text{Mo}_3\text{S}_4\text{@HSSZ-39}$ model. The reaction energies (ΔE) and activation barriers (E_a) were defined as the absolute differences between the final states and initial states, and transition states and initial states, respectively. The climbing image nudged elastic band (CI-NEB) method [39] and the improved dimer method [40] were employed to locate the transition states. Atomic charges were computed via the Bader charge analysis [41].

3. Results and discussions

3.1. Catalyst characterizations

As schematically shown in Fig. 1, the $\text{MoS}_x\text{@HSSZ-39}$ (the Mo content of all $\text{MoS}_x\text{@HSSZ-39}$ in this paper is ~3 wt.% unless otherwise stated) catalyst with MoS_x clusters located at cage of HSSZ-39 zeolite was obtained by two-step solid-phase exchange and sulfuring method (details see Section 2.2). The Mo content of $\text{MoS}_y\text{/HSSZ-39}$ ($\text{MoS}_y\text{/HSSZ-39}$ is represented by $\text{MoS}_2\text{/HSSZ-39}$ in all Graphics and Tables) and $\text{MoS}_x\text{@HSSZ-39}$ are analyzed as 2.93 wt.% and 2.95 wt.%, respectively, by ICP-OES (Table S1), which is consistent with Mo content of feed. As shown in Fig. 2(a), both $\text{MoS}_y\text{/HSSZ-39}$ and $\text{MoS}_x\text{@HSSZ-39}$ maintain intact AEI framework diffraction peaks and appear no-extra peaks, but the intensity of structural characteristic peaks slightly reduces, compared with fresh HSSZ-39 zeolite. Relative crystallinity is calculated to be 97% for $\text{MoS}_y\text{/HSSZ-39}$ and 87% for $\text{MoS}_x\text{@HSSZ-39}$.

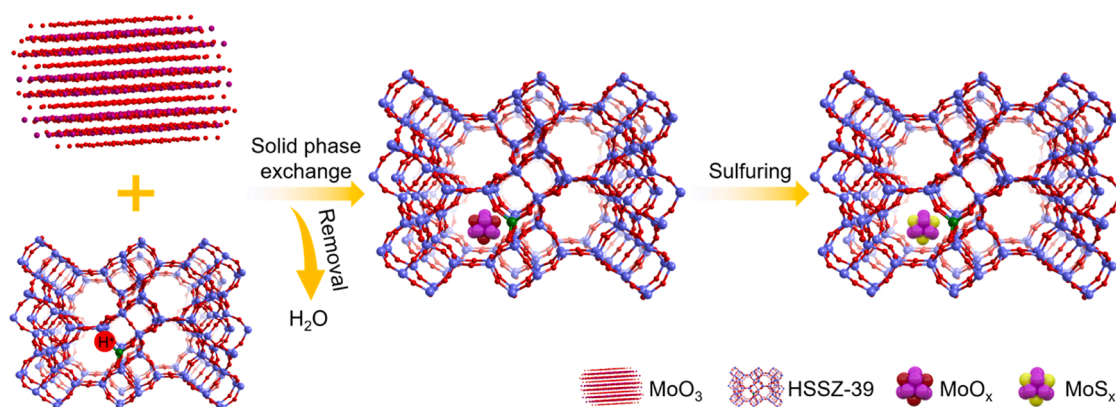


Fig. 1. Schematic show of the synthesis route for $\text{MoS}_x\text{@HSSZ-39}$, the green, red and blue balls in the framework of HSSZ-39 zeolite represent framework Al, O and Si atom, respectively.

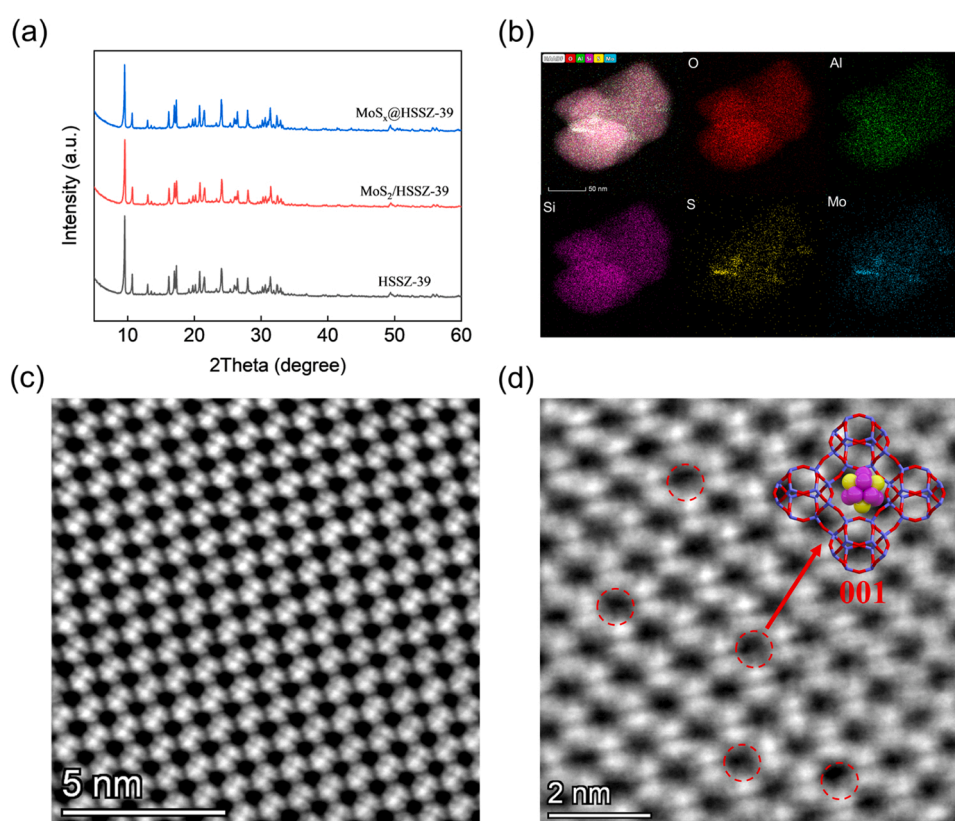


Fig. 2. (a) XRD patterns of HSSZ-39 zeolite, $\text{MoS}_2/\text{HSSZ-39}$ and $\text{MoS}_x\text{@HSSZ-39}$. (b) HAADF-STEM images and element distribution of O, Al, Si, S and Mo of $\text{MoS}_x\text{@HSSZ-39}$. (c) Spherical-aberration Corrected Scanning Transmission Electron Microscope-Integrated Differential Phase Contrast (STEM-IDPC) image of pure HSSZ-39 zeolite and (d) $\text{MoS}_x\text{@HSSZ-39}$, filler in red dotted circle represented MoS_x clusters.

via comparing the sum of the peak intensity at 2θ of 9.6, 17, 17.3, 20.8, 24.1 and 31.4° of sample with that of fresh HSSZ-39 zeolite defined as 100% [21]. No appearance of extra XRD peaks explains that the Mo species are highly dispersed on the external surface or in channel of HSSZ-39 zeolite. Naturally both slight reduction in relative crystallinity of $\text{MoS}_2/\text{HSSZ-39}$ and $\text{MoS}_x\text{@HSSZ-39}$ are primarily attributed to the introduction of Mo species. As seen in Figure S1, it is obvious that both $\text{MoS}_2/\text{HSSZ-39}$ and $\text{MoS}_x\text{@HSSZ-39}$ zeolite show identical micromorphology to pure HSSZ-39 zeolite, consistent with the result of XRD. The lattice fringes of layered MoS_2 with particle size of ~ 8 nm, is definitely loaded on the external surface of HSSZ-39 zeolite (0.38 nm of cage size) in HR-TEM image of $\text{MoS}_2/\text{HSSZ-39}$ (Figure S2). Therefore, the MoS_2 clusters are highly dispersed on the external surface of HSSZ-39 zeolite

in $\text{MoS}_2/\text{HSSZ-39}$. Both Mo and S elements are uniformly dispersed on $\text{MoS}_x\text{@HSSZ-39}$ (Fig. 2(b)).

The IDPC imaging technology could image light atoms under low irradiation dose and perform non-destructive imaging of zeolite channel structure. The microcosmic appearances for crystal face (001) of fresh SSZ-39 zeolite and $\text{MoS}_x\text{@HSSZ-39}$ were obtained, respectively, as shown in Fig. 2(c, d). The cages of zeolite in $\text{MoS}_x\text{@HSSZ-39}$ are evenly filled with the MoS_x clusters (in red circle) [42], compared with pure HSSZ-39 zeolite. The specific surface area of $\text{MoS}_x\text{@HSSZ-39}$ ($424 \text{ m}^2/\text{g}$, BET) is much smaller than that of HSSZ-39 zeolite ($510 \text{ m}^2/\text{g}$), which is attributed that some cages of zeolite are filled with the MoS_x clusters, consistent that the MoS_x clusters are highly dispersed inside the zeolite in $\text{MoS}_x\text{@HSSZ-39}$.

In order to further understand the valence state and local coordination environment of Mo element on the external surface or in the cages of SSZ-39 zeolite, both XPS and EXAFS techniques were used to characterize MoS_2 +HSSZ-39, MoS_y /HSSZ-39 and MoS_x @HSSZ-39. The Mo $3d_{5/2}$ and Mo $3d_{3/2}$ binding energies (Figure S3) shift to lower position after vulcanization for MoS_y /HSSZ-39 and MoS_x @HSSZ-39 [43], it is determined that MoO_3 is fully vulcanized during synthesis of both MoS_y /HSSZ-39 and MoS_x @HSSZ-39. As shown in Fig. 3(a), the absorption edge of the Mo K-edge of MoS_y /HSSZ-39 appears similar energy level compared with MoS_2 +HSSZ-39. This result denotes that the molybdenum in MoS_y /HSSZ-39 and MoS_2 +HSSZ-39 have identical valence state [44]. No shift of Mo $3d_{5/2}$ and Mo $3d_{3/2}$ binding energy in MoS_y /HSSZ-39 compared with MoS_2 +HSSZ-39 also affirms this view. Moreover, massive lattice fringes of layered MoS_2 are observed in HR-TEM image of MoS_y /HSSZ-39 (Figure S2), resulting that the MoS_2 is dispersed on the external surface of SSZ-39 zeolite in MoS_y /HSSZ-39 (MoS_y /HSSZ-39 is represented by MoS_2 /HSSZ-39, vide infra). Both the absorption edge of the Mo K-edge (Fig. 3(a)) and binding energies of Mo $3d_{5/2}$ and Mo $3d_{3/2}$ (Figure S3) of MoS_x @HSSZ-39 shift a positive energy level compared with MoS_2 +HSSZ-39, which indicates that the valence state of molybdenum in MoS_x @HSSZ-39 is higher than that in MoS_2 +HSSZ-39. This result is mainly related to the fact that MoS_x clusters are firmly located at cages of zeolite owing to strong interaction between Mo of MoS_x clusters and O on framework of zeolite [15,44]. Compared with Mo-S bond, the shared electron pair of Mo-O bond is more inclined to deviate from Mo atom on account of the greater electronegativity on O atom than S atom.

The Fourier-transformed EXAFS spectra of MoS_2 +HSSZ-39, MoS_2 /HSSZ-39 and MoS_x @HSSZ-39 are shown in Fig. 3(b), the corresponding

fitting results and parameters are shown Table 1. The nonlinear least-squares fitting of the Mo-S and Mo-Mo shells for MoS_2 /HSSZ-39 are shown in Figure S4 and MoS_x @HSSZ-39 are shown in Fig. 3(c, d). The bond length of both Mo-S and Mo-Mo bond in three samples are similar with slightly different coordination number. It is speculated that part migration of Mo to surface cages of SSZ-39 zeolite, during the heat treatment of MoS_2 /HSSZ-39, causes difference in coordination number of Mo-S and Mo-Mo between MoS_2 +HSSZ-39 (6, 6) and MoS_2 /HSSZ-39 (~ 3.6 , ~ 3.4). The fact that BET specific surface area of MoS_2 /HSSZ-39 ($463 \text{ m}^2/\text{g}$) is between MoS_x @HSSZ-39 ($424 \text{ m}^2/\text{g}$) and HSSZ-39 zeolite ($510 \text{ m}^2/\text{g}$) sidelines that part Mo species migrate to cages of SSZ-39 zeolite during the preparation of MoS_2 /HSSZ-39. It is interesting that the coordination numbers of Mo-S and Mo-Mo in MoS_x @HSSZ-39, ~ 4.3 and ~ 2.7 , are higher and lower than those of MoS_2 /HSSZ-39, respectively, which results from confinement effect of cages in SSZ-39 zeolite to MoS_x clusters, i.e. the additional coordination of zeolitic oxygen to the

Table 1

Mo K-edge EXAFS data for the Mo-based catalysts.^a

Samples	Scattered	Shell	R (\AA) ^b	CN ^c	σ^2 (\AA^2) ^d
MoS_2 +HSSZ-39	Mo	Mo-S	2.41	6	0.0018
		Mo-Mo	3.16	6	0.0022
MoS_2 /HSSZ-39	Mo	Mo-S	2.41	3.6 ± 0.2	0.0025
		Mo-Mo	3.16	3.4 ± 0.5	0.0030
MoS_x @HSSZ-39	Mo	Mo-S	2.40	4.3 ± 0.3	0.0035
		Mo-Mo	3.16	2.7 ± 0.7	0.0036

a: The R-factor of fitting in MoS_2 /HSSZ-39, MoS_x @HSSZ-39 were 0.004 and 0.005, respectively; b: bond length; c: coordination number; d: Debye-Waller factor.

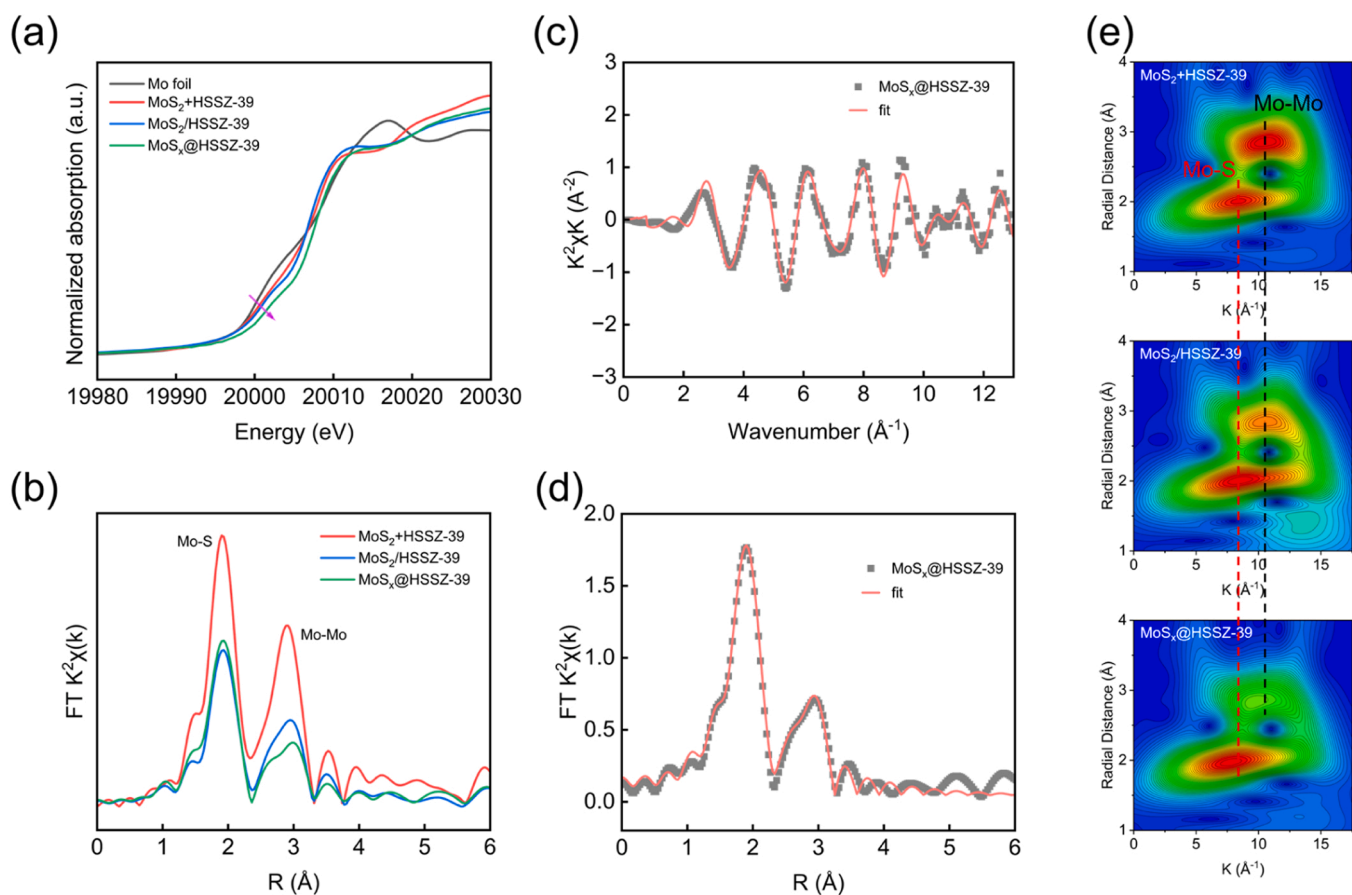


Fig. 3. (a) Mo K-edge XANES spectroscopy of Mo foil, MoS_2 +HSSZ-39, MoS_2 /HSSZ-39, MoS_x @HSSZ-39. (b) The FT-EXAFS spectra of MoS_2 +HSSZ-39, MoS_2 /HSSZ-39 and MoS_x @HSSZ-39. (c, d) Results of Mo K-edge EXAFS data fitting for MoS_x @HSSZ-39. (e) WT-EXAFS spectra of MoS_2 +HSSZ-39, MoS_2 /HSSZ-39 and MoS_x @HSSZ-39.

MoS_x clusters. As shown in Fig. 3(e), both the Mo-S and Mo-Mo bonds of MoS_x@HSSZ-39 shift to lower K value compared with that of MoS₂+HSSZ-39, which is related to different local coordination environment of molybdenum in cages of HSSZ-39 and formation of partial Mo-O bonds for MoS_x@HSSZ-39 catalyst [15,45].

In addition, the peak intensity of Mo 3d binding energy decreases in

turn MoS₂+HSSZ-39 > MoS₂/HSSZ-39 > MoS_x@HSSZ-39, owing to the depth of Mo species in SSZ-39 zeolite, in agreement with embedding of MoS_x clusters in cages of SSZ-39 zeolite in MoS_x@HSSZ-39. As listed in Table S2, the difference in Mo/S ratios among MoS₂+HSSZ-39 (0.41), MoS₂/HSSZ-39 (0.63) and MoS_x@HSSZ-39 (1.20) is explained by the fact that the MoS_x clusters in cage of MoS_x@HSSZ-39 are partly

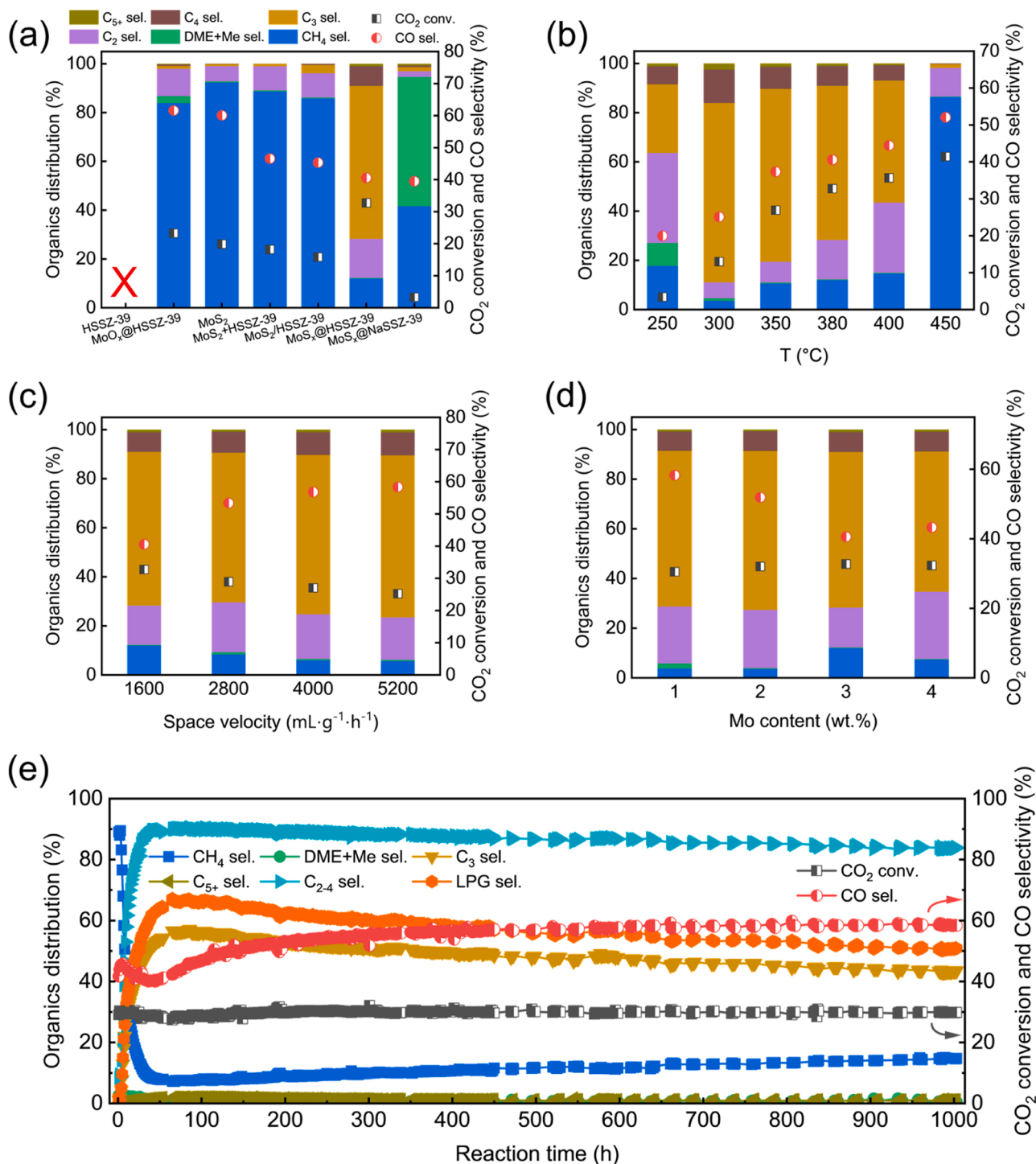


Fig. 4. Catalytic performance for CO₂ hydrogenation with the mixture of 23% CO₂/69% H₂/8% Ar as reaction gases (the catalyst MoS_x@HSSZ-39 reached a stable state after pretreatment at 380 °C, 4 MPa and 1600 mL g⁻¹·h⁻¹ for ~40 hours and other catalysts reached a stable state very fast, generally less than 5 h). (a) Commercial HSSZ-39 zeolite, MoO_x@HSSZ-39, commercial MoS₂, MoS₂+HSSZ-39, MoS₂/HSSZ-39, MoS_x@HSSZ-39 (380 °C, 4 MPa and 1600 mL g⁻¹·h⁻¹) and MoS_x@NaSSZ-39 (250 °C, 4 MPa, 1600 mL g⁻¹·h⁻¹). (b) Effect of reaction temperature (4 MPa and 1600 mL g⁻¹·h⁻¹) and (c) Effect of space velocity (380 °C, 4 MPa) on the catalytic property of MoS_x@HSSZ-39. (d) Effect of Mo content on catalytic performance of MoS_x@HSSZ-39 (380 °C, 4 MPa, 1600 mL g⁻¹·h⁻¹). (e) Catalytic stability test of MoS_x@HSSZ-39 (380 °C, 4 MPa, 1600 mL g⁻¹·h⁻¹). (DME+Me sel.: the selectivity to mixture of dimethyl ether and methanol).

coordinated with the framework oxygen of zeolite.

3.2. Catalytic CO₂ hydrogenation to C₂₋₄ hydrocarbons

Fig. 4(a) shows the data of the CO₂ hydrogenation reaction obtained on different catalysts. The HSSZ-39 zeolite is obviously unable to activate CO₂. Therefore, the molybdenum species in the catalysts become the protagonist to activate CO₂. Though the MoO_x species in zeolite could unexpectedly activate CO₂, but the major products are CO and CH₄ over MoO_x@HSSZ-39 catalyst. Over the commercial MoS₂, the CO selectivity is up to 60% and CH₄ selectivity in organic products reaches 92% at 19.9% of CO₂ conversion. The catalysts MoS₂+HSSZ-39 and MoS₂/HSSZ-39 show 47% and 45% of CO selectivity, 89% and 86% of CH₄ selectivity in organic products with 18.2% and 15.8% of CO₂ conversion for CO₂ hydrogenation reaction, respectively, similar to commercial MoS₂, indicating the MoS₂ is the major active site for the CO₂ hydrogenation over both MoS₂+HSSZ-39 and MoS₂/HSSZ-39 [46].

Using the catalyst MoS_x@HSSZ-39 for CO₂ hydrogenation, the CO selectivity is less than 40% and C₂₋₄ hydrocarbons in organic products is up to 87% (16% of C₂, 63% of C₃ and 8% of C₄ hydrocarbons) with 32.7% of CO₂ conversion. The significant difference in catalytic properties between the MoS_x@HSSZ-39 and MoS₂/HSSZ-39 is mainly attributed to the unique structure of MoS_x clusters located in cages of HSSZ-39 zeolite. Interestingly, the products over MoS_x@NaSSZ-39 for CO₂ hydrogenation are major CH₃OH (~53%) and small amount of dimethyl ether and C₂₋₄ hydrocarbons, coincident with our previous work [15]. In a controlled experiment, methanol to hydrocarbons (MTH) is performed over HSSZ-39 and 92% C₂₋₄ hydrocarbons with 100% conversion of methanol are observed, as shown in Figure S5, similar to the catalytic performance of MoS_x@HSSZ-39 (88% C₂₋₄ hydrocarbons with 100% conversion of methanol). It reveals that the CO₂ is firstly converted into methanol over MoS_x clusters, then the methanol is further hydrogenated to C₂₋₄ hydrocarbons on zeolitic acid sites during the CO₂ hydrogenation over MoS_x@HSSZ-39. The reaction results of MoS_x@NaSSZ-39 mainly reflect the contribution of MoS_x clusters, leading to methanol as main product, while the catalyst MoS_x@HSSZ-39 shows the cooperative property of catalysis of MoS_x clusters and zeolitic acids, producing hydrocarbons [8].

Both the influence of reaction temperature and gas hourly space velocity (GHSV) of feed gas on the CO₂ hydrogenation over MoS_x@HSSZ-39 were investigated in detail. At low temperature of 250 °C, as shown in Fig. 4(b), minor CH₃OCH₃ and CH₃OH (9%) appear at low CO₂ conversion (3.4%), different from our previous work on Mo₃S₄@NaZSM-5 [15], reflecting the contribution of acid [21,47–50], neighboring the MoS_x sites, in MoS_x@HSSZ-39 zeolite. The low temperatures are beneficial to the dimethyl ether but unfavorable for methanol to hydrocarbons [5,17,51,52]. With the increase in temperature from 250 to 450 °C, both CO₂ conversion and CO selectivity remarkably increase from 3.4% and 20–41.4% and 52%, revealing the endothermic natures of CO₂ activation and RWGS reaction [5,31,53]. In term of organic products distribution, the CH₄ selectivity increases slowly from 3% to 15% with the increase of temperature from 300 to 400 °C but sharply increases to 86% at 450 °C. It is attributed to the characteristic of the kinetics of CO₂ methanation over MoS_x@HSSZ-39 catalyst. The C₂₋₄ hydrocarbons selectivity in organic products is always more than 80% with the temperature increased from 300 to 400 °C. At 300 °C, the selectivity to C₂₋₄ hydrocarbons in organic products reaches 95%, among them, 73% is propane, at 13.0% of CO₂ conversion.

The effects of GHSV of feed gas on CO₂ hydrogenation over MoS_x@HSSZ-39 are shown in Fig. 4(c). A certain decrease in the CO₂ conversion is observed, from 32.7% to 25.2% with more than 3 times increase in GHSV, from 1600 to 5200 mL g⁻¹·h⁻¹. Seemingly, it is not too much the influence of the reduction in contact time [28,53]. The unique structure of the catalyst MoS_x@HSSZ-39 with the zeolitic framework surrounding the MoS_x clusters is responsible for the unique properties of catalysis. The selectivities to CO, CH₄, C₂₋₄ hydrocarbons

in organic products show complicated changes, in relatively small amplitudes, with the space velocity increasing from 1600 to 5200 mL g⁻¹·h⁻¹. The optimized reaction temperature and space velocity should be 380 °C and 1600 mL g⁻¹·h⁻¹.

The effect of Mo content on CO₂ hydrogenation over MoS_x@HSSZ-39 was also explored and results are shown in Fig. 4(d). Interestingly, the Mo contents of 1–4 wt.% show similar catalytic performance for CO₂ conversion. The sample of 3 wt.% Mo gives the highest CO₂ conversion (32.7%). The CO selectivity displays a U-shaped curve with the increase of Mo content from 1–4 wt.% with the maximum (58%) at 1 wt.% and the minimum (40%) at 3 wt.% Mo content. With different Mo content, the selectivity of C₂₋₄ hydrocarbons in organic products always remains over 85% and the one with 3 wt.% Mo is the best for highly selective conversion of CO₂ to C₂₋₄ hydrocarbons. Fig. 4(e) depicts the results of the stability test over the MoS_x@HSSZ-39 for CO₂ hydrogenation (380 °C, 4 MPa and 1600 mL g⁻¹·h⁻¹). After 1000 hours on stream, the CO₂ conversion remains almost unchanged (~30%), while the C₃, C₂₋₄ hydrocarbons and LPG selectivity in organic products are more than 43%, 85% and 50%, respectively. The catalytic performance of some bifunctional catalysts for CO₂ hydrogenation to C₂₋₄ hydrocarbons were listed in Table S3, the MoS_x@HSSZ-39 catalyst shows excellent stability of 1000 h compared with listed catalysts. The selectivity to CO over MoS_x@HSSZ-39 is also lower than that of some catalysts under identical reaction temperature (653 K).

The XRD results of spent MoS_x@HSSZ-39 are given in Figure S6, showing complete AEI characteristic peaks of SSZ-39 zeolite and no other peaks identified, demonstrating that the structure of HSSZ-39 zeolite is maintained and the MoS_x still remains highly dispersion without any agglomeration after reaction, as evidenced by the STEM-IDPC image (Figure S7) of spent MoS_x@HSSZ-39.

3.3. Catalytic CO hydrogenation to propane and LPG

More interestingly, the MoS_x@HSSZ-39 catalyst also shows outstanding activity for CO hydrogenation. Generally, the CO conversion is significantly enhanced from 5% to 84% with the increase of temperature from 250 to 400 °C, with CO/2H₂ as reactant. The selectivity to C₂₋₄ hydrocarbons in organic products increases with the increase of temperature from 250 to 350 °C and reaches maximum value at 350 °C (96% of C₂₋₄, 85% of LPG and 75% of propane in organic products). Under the reaction conditions, the CO₂ selectivity remains unaltered and close to 50%, implying little water formed during the reaction and RWGS was neglectable, as shown in Fig. 5(a).

The influence of space velocity is shown in Fig. 5(b), with the increase of GHSV of feed gas from 1600 to 9600 mL g⁻¹·h⁻¹. Similarly, the CO₂ selectivity remains basically unchanged and, in the meantime, the selectivity to propane in organic products slightly decreases. The results of stability evaluation of MoS_x@HSSZ-39 catalyst for the CO hydrogenation are shown in Fig. 5(c) (350 °C, 4 MPa, 1600 mL g⁻¹·h⁻¹). The CO conversion gradually decreases from 61% to 22% in the first ~100 h and remains stable hereafter. The CO₂ selectivity are constrained within 45%. In addition, the selectivities to C₂₋₄, LPG or propane in organic products keep over 95%, 83% or 74%, respectively.

3.4. Reaction mechanism of CO₂/CO hydrogenation

The reaction of CO₂ and CO hydrogenation over MoS_x@HSSZ-39 under the reaction conditions of CO₂/3H₂, 3 MPa, 380 °C and CO/2H₂, 3 MPa, 350 °C were monitored by operando Diffused Reflectance Infrared Fourier Transform Spectroscopy (DRIFTS), in order to understand the reaction mechanism. As shown in Fig. 6(a), the peak at 2882 cm⁻¹ is assigned to *CH₃O species and the peaks between 2100 and 2050 cm⁻¹ are determined to *CO species [2,15,54]. At the beginning of reaction, these peaks emerge and their intensities increase gradually with time, indicating that both *CH₃O and *CO species are generated in the reaction and their concentration increases with time to

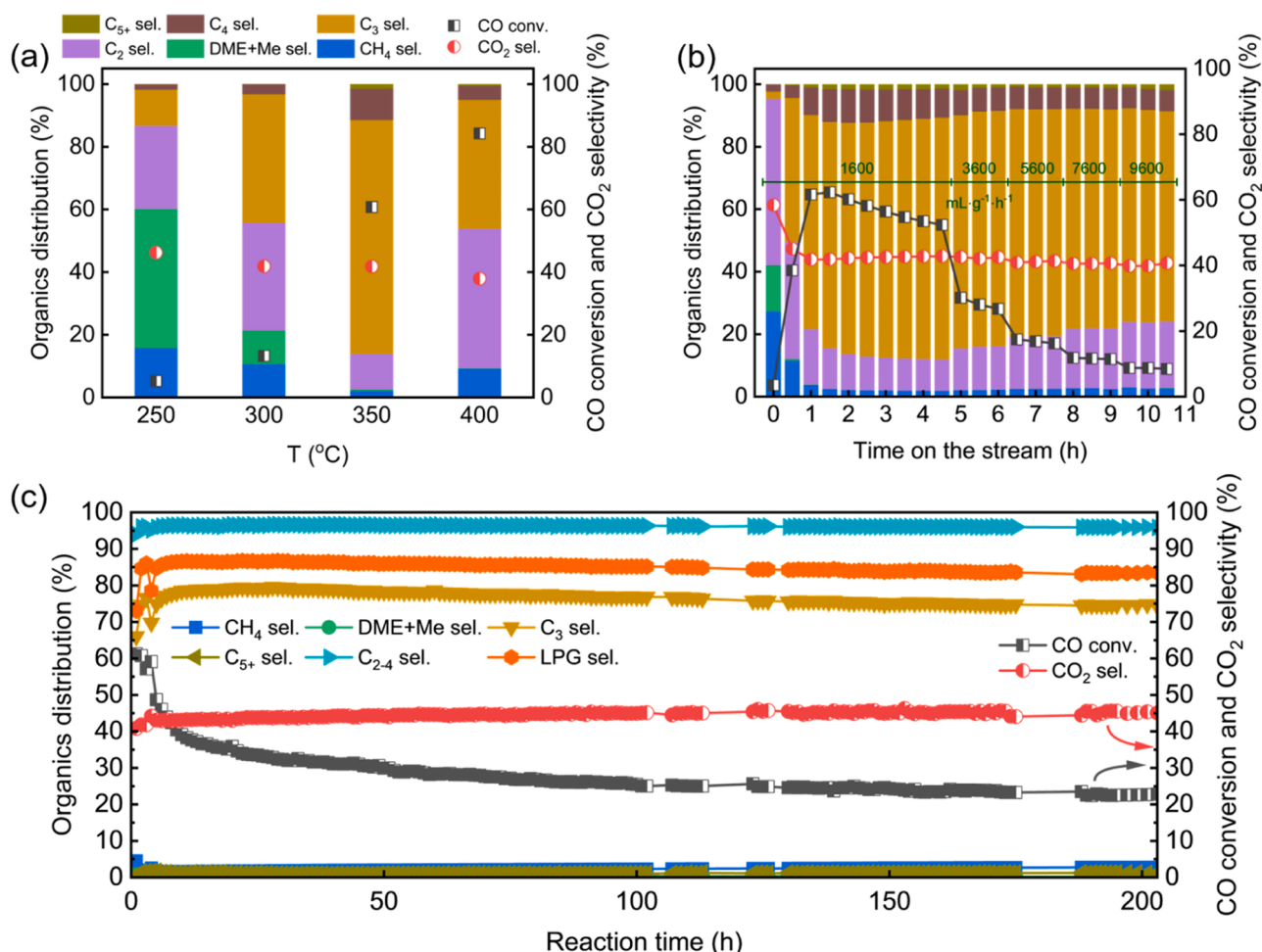


Fig. 5. Evaluation of catalytic activity of MoS_x@HSSZ-39 for CO hydrogenation with feed gas of 32% CO, 64% H₂ and 4% Ar. (a) Effect of reaction temperatures (4 MPa, 1600 mL g⁻¹ h⁻¹). (b) Effect of GHSV (350 °C, 4 MPa). (c) Stability test of MoS_x@HSSZ-39 catalyst (350 °C, 4 MPa, 1600 mL g⁻¹ h⁻¹). (DME+Me sel.: the selectivity to mixture of dimethyl ether and methanol).

a stable level. Combining the fact that massive CH₃OH appears during CO₂ hydrogenation over MoS_x@NaSSZ-39 (Fig. 4(a)), it is concluded that CO₂ is converted into the *CO intermediate and further hydrogenated into CH₃OH over the MoS_x clusters, consistent with our previous result [15]. High-efficient conversion of CO to propane further demonstrates that *CO is a key intermediate for CO₂ hydrogenation to CH₃OH over MoS_x clusters. The unsaturated =C-H, C-C stretching vibrations and methylene bending band -CH₂- are also observed during the reaction [15,55,56], as shown in Fig. 6(a). Moreover, both the signals of C-C and -CH₂- increase with the time, demonstrating that the alkenes are formed on the Brønsted acid sites in HSSZ-39 zeolite via the hydrocarbon pool (HCP) mechanism [22] (Figure S5) and further hydrogenated into alkanes during the reaction of CO₂ over MoS_x@HSSZ-39. As shown in Fig. 6(b), all peaks of the *CH₃O, =C-H, -CH₂- and C-C species appear and increase with time during the hydrogenation of CO reaction. Similarly, the CO firstly is converted into CH₃OH on MoS_x clusters and the CH₃OH intermediate is subsequently hydrogenated into propane on the Brønsted acid sites in HSSZ-39 zeolite.

Based on the results, the catalyst models are schematically summarized and shown in Fig. 6(c). Compared with the MoS₂+HSSZ-39 or MoS₂/HSSZ-39, the unique structure of MoS_x@HSSZ-39 brings about the synergy among the molybdenum sulfide clusters and zeolite acid sites constituting the intimate cooperation of bifunctional catalyst. CO₂ and CO are hydrogenated into C₂₋₄ hydrocarbons over MoS_x@HSSZ-39 via the methanol-intermediate process: CO₂ or CO are firstly converted into CH₃OH over MoS_x clusters via the CO-hydrogenation and which is

further rapidly converted into C₂₋₄ hydrocarbons over the Brønsted acid sites of HSSZ-39 zeolite via the MTH process (Fig. 6(d)). In addition, as shown in Figure S8, the MoS_x@HSSZ-39 is also highly active for conversion of the mixture of CO₂ and CO into propane (73%), LPG (83%) and C₂₋₄ hydrocarbons (94%) during 100 h on stream. The existence of CO in reactant could be helpful to inhibit the slow uptrend of CO selectivity with stable CO₂ conversion during the CO₂ hydrogenation reaction in long time of reaction (Fig. 4(e)). The strong Brønsted acid sites and narrow channels of HSSZ-39 zeolite effectively inhibit the formation of aromatic HCP species [57], thus significantly decreasing the contribution of aromatic-based cycle, while enhancing the hydrocarbon-pool-based cycle under high H₂ pressure for a high selectivity to propane in organic products [58–60].

In order to get deeper insight into the origin of superior catalytic activity over MoS_x@HSSZ-39, the process of CO₂ hydrogenation was further investigated by DFT calculations. As shown in Fig. 7(a), the representative 8-membered ring (8-MR) of the repeated AEI unit in HSSZ-39 can be a great container for accommodating the MoS_x species. On that account, a polyhedral Mo₃S₄ cluster (Figure S9) is placed into the 8-MR to construct an encapsulated model catalyst, which is labeled as Mo₃S₄@HSSZ-39 (Fig. 7(b)). Meanwhile, we find an intensive charge transfer between the zeolite and Mo₃S₄ cluster (Figure S10), leading to the cluster positively charged (+1.26 |e|) (Table S4). In this way, the whole process of CO₂ hydrogenation proceeded on the Mo₃S₄^{δ+} site is highly feasible. As reported, the formation of hydrocarbons followed two successive steps in which carbon dioxide is first hydrogenated to

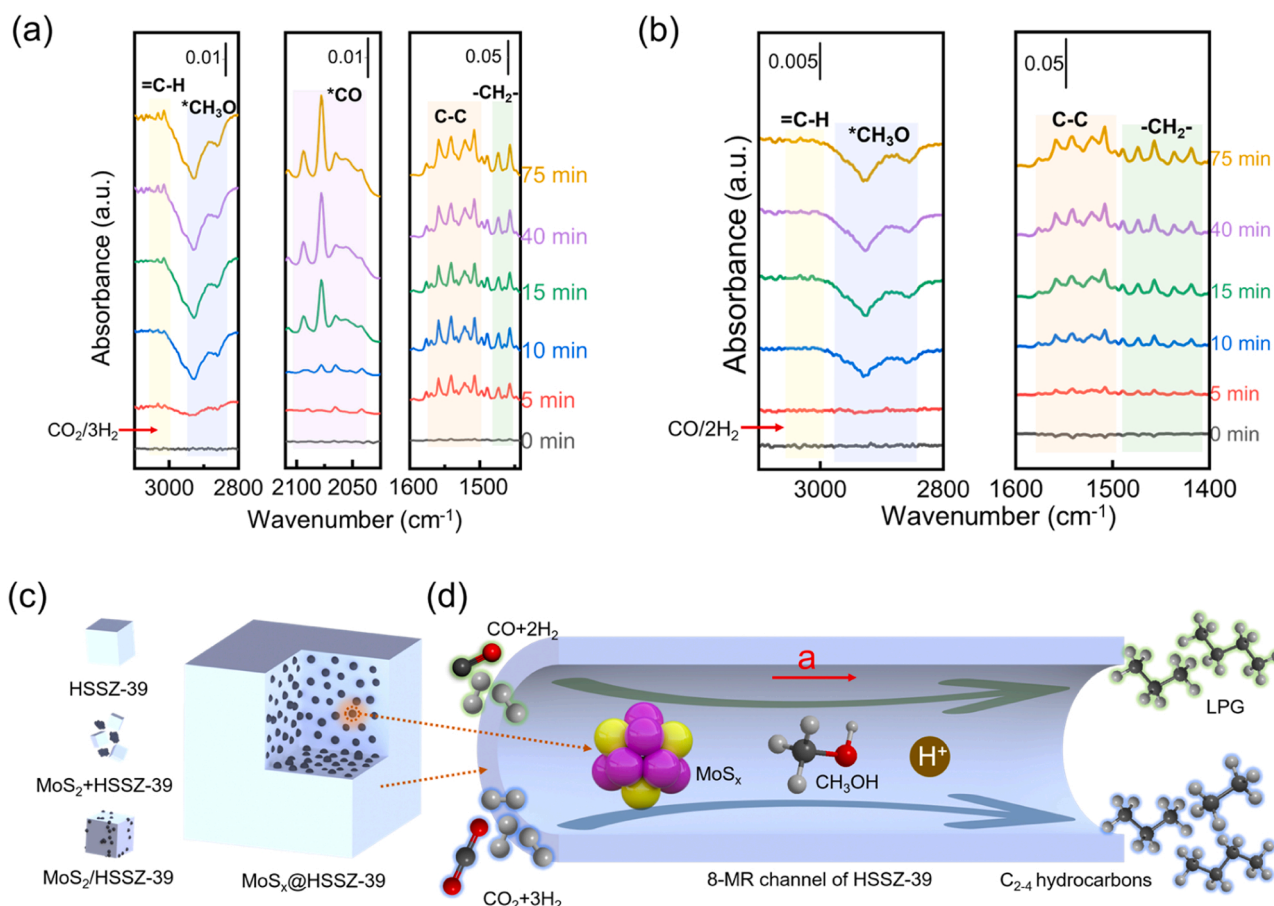


Fig. 6. Operando DRIFT spectra of $\text{MoS}_x\text{@HSSZ-39}$ catalyst: (a) under continuous reaction of CO_2 hydrogenation ($\text{CO}_2/3\text{H}_2$, 3 MPa, 380°C); (b) under continuous reaction of CO hydrogenation ($\text{CO}/2\text{H}_2$, 3 MPa, 350°C). (c) Catalyst models of HSSZ-39, $\text{MoS}_2\text{+HSSZ-39}$, $\text{MoS}_2\text{/HSSZ-39}$ and $\text{MoS}_x\text{@HSSZ-39}$ (light blue brick and black sphere represent zeolite and $\text{MoS}_2\text{/MoS}_x$, respectively). (d) Schematic show of the reaction process of CO_2 or CO hydrogenation over the $\text{MoS}_x\text{@HSSZ-39}$ catalyst.

methanol, and then converted to hydrocarbons via the MTH process [22]. Given that the hydrocarbon pool involved in the MTH process is rather complicated, herein, only the first step of CO_2 hydrogenation to methanol is considered and the energy profile is depicted in Fig. 7(c). In the primary stage, CO_2 is first activated on the Mo_3S_4 cluster in an exothermic way ($\Delta E = -0.50$ eV). Afterwards, the adsorbed $^*\text{CO}_2$ would be either hydrogenated to $^*\text{HCOO}$ or $^*\text{COOH}$, or directly dissociated to $^*\text{CO}$ and $^*\text{O}$ species. The corresponding initial states, transition states and final states are shown in Figure S11-S13. It is found the activation barriers for the generation of $^*\text{COOH}$ and $^*\text{HCOO}$ were 0.59 and 0.88 eV, respectively. In contrast, the activation barrier for the direct dissociation of $^*\text{CO}_2$ is lower (0.40 eV). This indicates the formation of $^*\text{CO}$ species is more facile, which is in good agreement with the operando DRIFT analysis (Fig. 6(a)). In addition, the generated $^*\text{CO}$ would rather be hydrogenated to $^*\text{HCO}$ ($E_a = 0.46$ eV, Figure S14) than desorb from the catalyst surface ($\Delta E = 0.99$ eV), and the further hydrogenation of $^*\text{HCO}$ to $^*\text{H}_2\text{CO}$, $^*\text{H}_3\text{CO}$ and CH_3OH is more advantageous in the thermodynamic aspect. These results also well account for the outstanding performance for the formation of hydrocarbons from syngas (*vide supra*). In light of this, the most plausible pathway for CO_2 hydrogenation to methanol over $\text{Mo}_3\text{S}_4\text{@HSSZ-39}$ follows $\text{CO}_2 \rightarrow \text{CO} \rightarrow \text{HCO} \rightarrow \text{H}_2\text{CO} \rightarrow \text{H}_3\text{CO} \rightarrow \text{CH}_3\text{OH}$, and all the key intermediates are presented in Fig. 7(d).

4. Conclusions

To sum up, the direct conversion of CO_2 or CO to C_{2-4} hydrocarbons with superior catalytic performance is realized by successfully

constructing an intimate bifunctional $\text{MoS}_x\text{@HSSZ-39}$ catalyst with MoS_x clusters positioned into the cages of SSZ-39 zeolite through a two-step method of solid-phase exchange and sulfurization. Characterizations as well as DFT studies confirm the electron transfer between the zeolite and MoS_x , resulting in a positively-charged cluster. As such, CO_2 and CO molecules can be effectively activated on the MoS_x clusters and then converted into CH_3OH , after which the C-C bond formation is enabled on the neighboring Brønsted acid sites within the HSSZ-39 zeolite. As for CO_2 hydrogenation, CO_2 conversion reaches to 32.7% with the selectivity exceeding 87% to C_{2-4} hydrocarbons in organic products. The $\text{MoS}_x\text{@HSSZ-39}$ catalyst exhibits excellent stability of catalytic performance for CO_2 hydrogenation during the 1000 h on stream. While for CO hydrogenation, the selectivity to C_{2-4} hydrocarbons, LPG or propane in organic products are more than 95%, 83% or 74%, respectively, at more than 22% of CO conversion during 200 h on stream. The synergistic cooperation between the MoS_x clusters and the zeolitic acid sites is pivotal to the excellent catalytic performance for CO_2 and CO conversion over the $\text{MoS}_x\text{@HSSZ-39}$.

CRedit authorship contribution statement

Yuchi Liu: Investigation, Formal analysis, Data curation. **Yan Zhu:** Methodology, Investigation, Formal analysis. **Taotao Zhao:** Writing – original draft, Investigation, Formal analysis, Data curation. **Nianhua Xue:** Software, Resources, Project administration, Methodology, Investigation, Conceptualization. **Gui Liu:** Methodology, Investigation, Data curation. **Chenyang Shen:** Software, Resources, Data curation. **Yuming Zhou:** Resources. **Deming Meng:** Investigation. **Feifei Mei:**

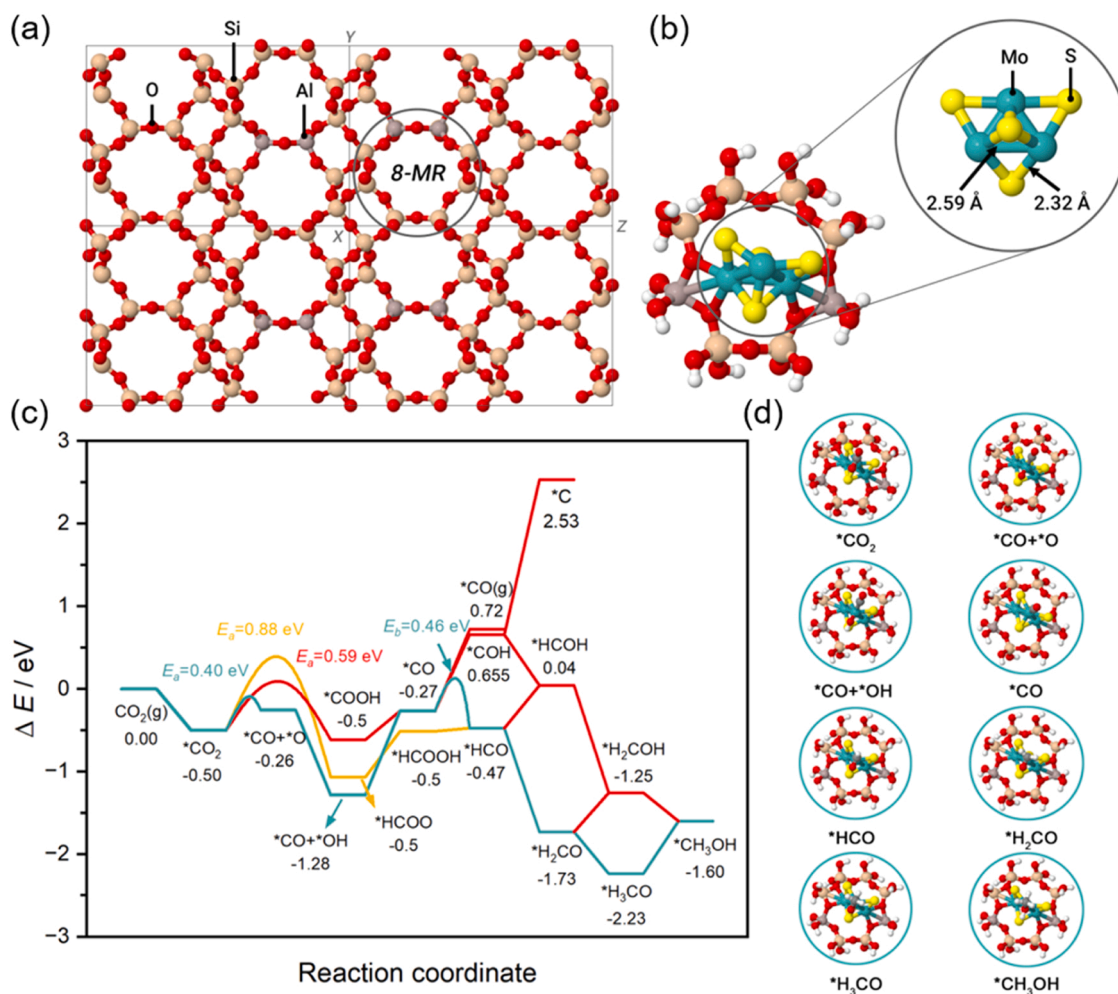


Fig. 7. DFT calculations. (a) The framework of HSSZ-39 zeolite, in which the circle marked the zig-zag 8-MR with double aluminum sites. (b) Optimized configuration of Mo₃S₄@HSSZ-39 with Mo₃S₄ cluster intercalated into the 8-MR. (c) Energy profile for the hydrogenation of CO₂ to methanol over Mo₃S₄@HSSZ-39. (d) All the possible intermediates involved in CO₂ hydrogenation to methanol over Mo₃S₄@HSSZ-39.

Investigation, Data curation. **Weiping Ding:** Writing – review & editing, Supervision, Resources, Project administration, Methodology, Investigation, Funding acquisition, Conceptualization. **Luming Peng:** Resources, Investigation, Data curation. **Xuefeng Guo:** Resources, Formal analysis. **Jun Yao:** Software, Investigation. **Qiang He:** Resources, Investigation. **Xiaofeng Qian:** Investigation.

Declaration of Competing Interest

The authors declare that they have no known competing financial interests or personal relationships that could have appeared to influence the work reported in this paper.

Data availability

Data will be made available on request.

Acknowledgements

This work was supported by the National Natural Science Foundation of China (21932004, 91963206, 21872067, 22172072, and 22072090) and the Ministry of Science and Technology of China (2021YFA1500301). The support from the NJU-HUACHANG Joint Institute of Meso Catalysis was also appreciated.

Appendix A. Supporting information

Supplementary data associated with this article can be found in the online version at [doi:10.1016/j.apcatb.2024.123936](https://doi.org/10.1016/j.apcatb.2024.123936).

References

- [1] P. Gao, S. Li, X. Bu, S. Dang, Z. Liu, H. Wang, L. Zhong, M. Qiu, C. Yang, J. Cai, W. Wei, Y. Sun, Direct conversion of CO₂ into liquid fuels with high selectivity over a bifunctional catalyst, *Nat. Chem.* 9 (2017) 1019–1024.
- [2] J. Hu, L. Yu, J. Deng, Y. Wang, K. Cheng, C. Ma, Q. Zhang, W. Wen, S. Yu, Y. Pan, J. Yang, H. Ma, F. Qi, Y. Wang, Y. Zheng, M. Chen, R. Huang, S. Zhang, Z. Zhao, J. Mao, X. Meng, Q. Ji, G. Hou, X. Han, X. Bao, Y. Wang, D. Deng, Sulfur vacancy-rich MoS₂ as a catalyst for the hydrogenation of CO₂ to methanol, *Nat. Catal.* 4 (2021) 242–250.
- [3] J. Wang, G. Zhang, J. Zhu, X. Zhang, F. Ding, A. Zhang, X. Guo, C. Song, CO₂ hydrogenation to methanol over In₂O₃-based catalysts: from mechanism to catalyst development, *ACS Catalysis* 11 (2021) 1406–1423.
- [4] J. Wei, Q. Ge, R. Yao, Z. Wen, C. Fang, L. Guo, H. Xu, J. Sun, Directly converting CO₂ into a gasoline fuel, *Nat. Commun.* 8 (2017) 15174.
- [5] R.-P. Ye, J. Ding, W. Gong, M.D. Argyle, Q. Zhong, Y. Wang, C.K. Russell, Z. Xu, A. G. Russell, Q. Li, M. Fan, Y.-G. Yao, CO₂ hydrogenation to high-value products via heterogeneous catalysis, *Nat. Commun.* 10 (2019) 5698.
- [6] W. Li, Y. Zhang, Y. Wang, W. Ran, Q. Guan, W. Yi, L. Zhang, D. Zhang, N. Li, T. Yan, Graphdiyne facilitates photocatalytic CO₂ hydrogenation into C₂+ hydrocarbons, *Appl. Catal. B: Environ.* 340 (2024) 123267.
- [7] E. de Smit, B.M. Weckhuysen, The renaissance of iron-based Fischer-Tropsch synthesis: on the multifaceted catalyst deactivation behaviour, *Chem. Soc. Rev.* 37 (2008) 2758–2781.

- [8] F. Jiao, J. Li, X. Pan, J. Xiao, H. Li, H. Ma, M. Wei, Y. Pan, Z. Zhou, M. Li, S. Miao, J. Li, Y. Zhu, D. Xiao, T. He, J. Yang, F. Qi, Q. Fu, X. Bao, Selective conversion of syngas to light olefins, *Science* 351 (2016) 1065–1068.
- [9] A.Y. Khodakov, W. Chu, P. Fongarland, Advances in the development of novel cobalt Fischer-Tropsch catalysts for synthesis of long-chain hydrocarbons and clean fuels, *Chem. Rev.* 107 (2007) 1692–1744.
- [10] Q. Zhang, J. Kang, Y. Wang, Development of novel catalysts for Fischer-Tropsch synthesis: tuning the product selectivity, *ChemCatChem* 2 (2010) 1030–1058.
- [11] Q. Yang, A. Skrypnik, A. Matvienko, H. Lund, M. Holena, E.V. Kondratenko, Revealing property-performance relationships for efficient CO₂ hydrogenation to higher hydrocarbons over Fe-based catalysts: statistical analysis of literature data and its experimental validation, *Appl. Catal. B: Environ.* 282 (2021) 119554.
- [12] M. Al-Dossary, A.A. Ismail, J.L.G. Fierro, H. Bouzid, S.A. Al-Sayari, Effect of Mn loading onto MnFeO nanocomposites for the CO₂ hydrogenation reaction, *Appl. Catal. B: Environ.* 165 (2015) 651–660.
- [13] J. Gross, G. Sadowski, Perturbed-chain SAFT: an equation of state based on a perturbation theory for chain molecules, *Ind. Eng. Chem. Res.* 40 (2001) 1244–1260.
- [14] P. Kaiser, R.B. Unde, C. Kern, A. Jess, Production of liquid hydrocarbons with CO₂ as carbon source based on reverse water-gas shift and Fischer-Tropsch synthesis, *Chem. Ing. Tech.* 85 (2013) 489–499.
- [15] G. Liu, P. Liu, D. Meng, T. Zhao, X. Qian, Q. He, X. Guo, J. Qi, L. Peng, N. Xue, Y. Zhu, J. Ma, Q. Wang, X. Liu, L. Chen, W. Ding, CO_x hydrogenation to methanol and other hydrocarbons under mild conditions with Mo₃S₄@ZSM-5, *Nat. Commun.* 14 (2023) 513.
- [16] K. Li, J.G. Chen, CO₂ hydrogenation to methanol over ZrO₂-containing catalysts: insights into ZrO₂ induced synergy, *ACS Catalysis* 9 (2019) 7840–7861.
- [17] X. Jiang, X. Nie, X. Guo, C. Song, J.G. Chen, Recent advances in carbon dioxide hydrogenation to methanol via heterogeneous catalysis, *Chem. Rev.* 120 (2020) 7984–8034.
- [18] G. Noh, E. Lam, D.T. Bregante, J. Meyet, P. Šot, D.W. Flaherty, C. Copéret, Lewis acid strength of interfacial metal sites drives CH₃OH selectivity and formation rates on Cu-based CO₂ hydrogenation catalysts, *Angew. Chem. Int. Ed.* 60 (2021) 9650–9659.
- [19] L. Song, H. Wang, S. Wang, Z. Qu, Dual-site activation of H₂ over Cu/ZnAl₂O₄ boosting CO₂ hydrogenation to methanol, *Appl. Catal. B: Environ.* 322 (2023) 122137.
- [20] K. Sun, C. Shen, R. Zou, C.-j. Liu, Highly active Pt/In₂O₃-ZrO₂ catalyst for CO₂ hydrogenation to methanol with enhanced CO tolerance: the effects of ZrO₂, *Appl. Catal. B: Environ.* 320 (2023) 122018.
- [21] T. Zhao, Y. Wang, C. Sun, A. Zhao, C. Wang, X. Zhang, J. Zhao, Z. Wang, J. Lu, S. Wu, W. Liu, Direct synthesis of hierarchical binder-free ZSM-5 and catalytic properties for MTP, *Microporous Mesoporous Mater.* 292 (2020) 109731.
- [22] M. Bjørgen, S. Svelle, F. Joensen, J. Nerlov, S. Kolboe, F. Bonino, L. Palumbo, S. Bordiga, U. Olsbye, Conversion of methanol to hydrocarbons over zeolite H-ZSM-5: On the origin of the olefinic species, *J. Catal.* 249 (2007) 195–207.
- [23] X. Wu, S. Xu, W. Zhang, J. Huang, J. Li, B. Yu, Y. Wei, Z. Liu, Direct mechanism of the first carbon-carbon bond formation in the methanol-to-hydrocarbons process, *Angew. Chem. Int. Ed.* 56 (2017) 9039–9043.
- [24] G. Chen, J. Li, S. Wang, J. Han, X. Wang, P. She, W. Fan, B. Guan, P. Tian, J. Yu, Construction of single-crystalline hierarchical ZSM-5 with open nanoarchitectures via anisotropic-kinetics transformation for the methanol-to-hydrocarbons reaction, *Angew. Chem. Int. Ed.* 61 (2022) e202200677.
- [25] T. Fu, J. Shao, Z. Li, Catalytic synergy between the low Si/Al ratio Zn/ZSM-5 and high Si/Al ratio HZSM-5 for high-performance methanol conversion to aromatics, *Appl. Catal. B: Environ.* 291 (2021) 120098.
- [26] T. Sun, B.D.A. Levin, J.L.L. Guzman, A. Enders, D.A. Muller, L.T. Angenent, J. Lehmann, Rapid electron transfer by the carbon matrix in natural pyrogenic carbon, *Nat. Commun.* 8 (2017) 14873.
- [27] Z. Li, Y. Qu, J. Wang, H. Liu, M. Li, S. Miao, C. Li, Highly selective conversion of carbon dioxide to aromatics over tandem catalysts, *Joule* 3 (2019) 570–583.
- [28] S. Wang, L. Zhang, W. Zhang, P. Wang, Z. Qin, W. Yan, M. Dong, J. Li, J. Wang, L. He, U. Olsbye, W. Fan, Selective conversion of CO₂ into propene and butene, *Chem* 6 (2020) 3344–3363.
- [29] X. Wang, C. Zeng, N. Gong, T. Zhang, Y. Wu, J. Zhang, F. Song, G. Yang, Y. Tan, Effective suppression of CO selectivity for CO₂ hydrogenation to high-quality gasoline, *ACS Catal.* 11 (2021) 1528–1547.
- [30] M. Dusselier, M.A. Deimund, J.E. Schmidt, M.E. Davis, Methanol-to-olefins catalysis with hydrothermally treated zeolite SSZ-39, *ACS Catal.* 5 (2015) 6078–6085.
- [31] N. Martín, Z. Li, J. Martínez-Triguero, J. Yu, M. Moliner, A. Corma, Nanocrystalline SSZ-39 zeolite as an efficient catalyst for the methanol-to-olefin (MTO) process, *Chem. Commun.* 52 (2016) 6072–6075.
- [32] L. Wei, G.D. Meitzner, R. Ili, E. Iglesia, Raman and X-ray absorption studies of Mo species in Mo/H-ZSM5 catalysts for non-oxidative CH₄ reactions, *J. Catal.* 191 (2000) 373–383.
- [33] Y.-H. Kim, R.W. Borry III, E. Iglesia, Catalytic properties of Mo/HZSM-5 for CH₄ aromatization, *J. Ind. Eng. Chem.* 6 (2000) 72–78.
- [34] N. Liu, L. Nie, N. Xue, H. Dong, L. Peng, X. Guo, W. Ding, Catalytic ammonia synthesis over Mo nitride/ZSM-5, *ChemCatChem* 2 (2010) 167–174.
- [35] G. Kresse, J. Furthmüller, Efficiency of ab-initio total energy calculations for metals and semiconductors using a plane-wave basis set, *Comput. Mater. Sci.* 6 (1996) 15–50.
- [36] G. Kresse, J. Furthmüller, Efficient iterative schemes for ab initio total-energy calculations using a plane-wave basis set, *Phys. Rev. B* 54 (1996) 11169–11186.
- [37] J.P. Perdew, K. Burke, M. Ernzerhof, Generalized gradient approximation made simple, *Phys. Rev. Lett.* 77 (1996) 3865–3868.
- [38] P.E. Blöchl, Projector augmented-wave method, *Phys. Rev. B* 50 (1994) 17953–17979.
- [39] G. Henkelman, H. Jónsson, Improved tangent estimate in the nudged elastic band method for finding minimum energy paths and saddle points, *J. Chem. Phys.* 113 (2000) 9978–9985.
- [40] G. Henkelman, H. Jónsson, A dimer method for finding saddle points on high dimensional potential surfaces using only first derivatives, *J. Chem. Phys.* 111 (1999) 7010–7022.
- [41] R.F.W. Bader, A quantum theory of molecular structure and its applications, *Chem. Rev.* 91 (1991) 893–928.
- [42] L. Liu, M. Lopez-Haro, C.W. Lopes, S. Rojas-Buzo, P. Concepcion, R. Manzorro, L. Simonelli, A. Sattler, P. Serna, J.J. Calvino, A. Corma, Structural modulation and direct measurement of subnanometric bimetallic PtSn clusters confined in zeolites, *Nat. Catal.* 3 (2020) 628–638.
- [43] K.V.R. Chary, K.R. Reddy, G. Kishan, J.W. Niemantsverdriet, G. Mestl, Structure and catalytic properties of molybdenum oxide catalysts supported on zirconia, *J. Catal.* 226 (2004) 283–291.
- [44] W. Ding, S. Li, G.D. Meitzner, E. Iglesia, Methane conversion to aromatics on Mo/H-ZSM5: structure of molybdenum species in working catalysts, *J. Phys. Chem. B* 105 (2000) 506–513.
- [45] M. Xie, S. Tang, Z. Li, M. Wang, Z. Jin, P. Li, X. Zhan, H. Zhou, G. Yu, Intermetallic single-atom alloy In-Pd bimetallic for neutral electrosynthesis of ammonia from nitrate, *J. Am. Chem. Soc.* 145 (2023) 13957–13967.
- [46] S. Liu, H. Zhou, L. Zhang, Z. Ma, Y. Wang, Activated carbon-supported Mo-Co-K sulfide catalysts for synthesizing higher alcohols from CO₂, *Chem. Eng. Technol.* 42 (2019) 962–970.
- [47] Z. Shi, A. Bhan, Tuning the ethylene-to-propylene ratio in methanol-to-olefins catalysis on window-cage type zeolites, *J. Catal.* 395 (2021) 266–272.
- [48] P. Bollini, A. Bhan, Improving HSAPO-34 methanol-to-olefin turnover capacity by seeding the hydrocarbon pool, *ChemPhysChem* 19 (2018) 479–483.
- [49] V. Hulea, C. Cobzaru, S. Oprea, E. Dumitriu, The methanol-to-hydrocarbons conversion on SAPO molecular sieves. III, *Convers. Technol. Methanol-to-Hydrocarb. Rev. Chim.* 53 (2002) 776–779.
- [50] G. Chen, J. Li, S. Wang, J. Han, X. Wang, P. She, W. Fan, B.Y. Guan, J. Yu, P. Tian, Construction of single-crystalline hierarchical ZSM-5 with open nanoarchitectures via anisotropic-kinetics transformation for the methanol-to-hydrocarbons reaction, *Angew. Chem. Int. Ed.* (2022) e202200677.
- [51] J. Wei, R. Yao, Y. Han, Q. Ge, J. Sun, Towards the development of the emerging process of CO₂ heterogeneous hydrogenation into high-value unsaturated heavy hydrocarbons, *Chem. Soc. Rev.* 50 (2021) 10764–10805.
- [52] L. Guo, J. Sun, Q. Ge, N. Tsubaki, Recent advances in direct catalytic hydrogenation of carbon dioxide to valuable C₂₊ hydrocarbons, *J. Mater. Chem. A* 6 (2018) 23244–23262.
- [53] Z. Li, J. Wang, Y. Qu, H. Liu, C. Tang, S. Miao, Z. Feng, H. An, C. Li, Highly selective conversion of carbon dioxide to lower olefins, *ACS Catal.* 7 (2017) 8544–8548.
- [54] C. Deng, X. Qian, M. Lu, Q. Liu, T. Zhao, J. Yang, T. Chen, L. Dong, CO oxidation and NO reduction by CO over Sn⁴⁺ doped CeO₂ catalysts: Determination of active sites as well as commonness and differences, *Appl. Catal. B: Environ.* 333 (2023) 122791.
- [55] C. Deng, Y. Cui, J. Chen, T. Chen, X. Guo, W. Ji, L. Peng, W. Ding, Enzyme-like mechanism of selective toluene oxidation to benzaldehyde over organophosphoric acid-bonded nano-oxides, *Chin. J. Catal.* 42 (2021) 1509–1518.
- [56] K. Das, C. Kendall, M. Isabelle, C. Fowler, J. Christie-Brown, N. Stone, FTIR of touch imprint cytology: A novel tissue diagnostic technique, *J. Photochem. Photobiol. B: Biol.* 92 (2008) 160–164.
- [57] D.L.S. Nieskens, J.D. Lunn, A. Malek, Understanding the enhanced lifetime of SAPO-34 in a direct syngas-to-hydrocarbons process, *ACS Catal.* 9 (2019) 691–700.
- [58] S. Wang, L. Zhang, P. Wang, W. Jiao, Z. Qin, M. Dong, J. Wang, U. Olsbye, W. Fan, Highly selective hydrogenation of CO₂ to propane over GaZrO_x/H-SSZ-13 composite, *Nat. Catal.* 5 (2022) 1038–1050.
- [59] S.S. Arora, Z. Shi, A. Bhan, Mechanistic basis for effects of high-pressure H₂ cofeeds on methanol-to-hydrocarbons catalysis over zeolites, *ACS Catal.* (2019) 6407–6414.
- [60] S. Wang, Y. Chen, Z. Wei, Z. Qin, H. Ma, M. Dong, J. Li, W. Fan, J. Wang, Polymethylbenzene or alkene cycle? Theoretical study on their contribution to the process of methanol to olefins over H-ZSM-5 zeolite, *J. Phys. Chem. C* 119 (2015) 28482–28498.